Met. Mater. Int., Vol. 21, No. 3 (2015), pp. 429~439
doi: 10.1007/s12540-015-4499-2

Review Paper

Measurements of Microhardness During Transient Horizontal Directional Solidification of Al-Rich Al-Cu Alloys: Effect of Thermal Parameters, Primary Dendrite Arm Spacing and Al_2Cu Intermetallic Phase

André Santos Barros[1], Igor Alexsander Magno[2], Fabrício Andrade Souza[2], Carlos Alberto Mota[1], Antonio Luciano Moreira[1], Maria Adrina Silva[1], and Otávio Lima Rocha[1,2,*]

[1]Faculty of Mechanical Engineering, Federal University of Pará, UFPA, Augusto Corrêa Avenue 1, 66075-110, Belém, PA, Brazil
[2]Federal Institute of Education, Science and Technology of Pará, IFPA, Almirante Barroso Avenue 1155, 66093-020, Belém, PA, Brazil

(received date: 22 October 2014 / accepted date: 9 December 2014)

In this work, the effect of the growth rate (V_L) and cooling rate (T_R), primary dendritic arm spacing (λ_1) and Al_2Cu intermetallic phase on the microhardness was investigated during transient horizontal directional solidification of Al-3wt%Cu and Al-8wt%Cu alloys. Microstructural characterization of the investigated alloys was performed using traditional techniques of metallography, optical and SEM microscopy and X-Ray diffraction. The microhardness evolution as a function of the thermal and microstructural parameters (V_L, T_R, and λ_1) was evaluated using power and Hall-Petch type experimental laws, which were compared with other laws in the literature. In order to examine the effect of the Al_2Cu intermetallic phase, microhardness measurements were performed in interdendritic regions. Finally, a comparative analysis was performed between the experimental data of this work and theoretical models from the literature that have been proposed to predict primary dendrite arm spacing, which have been tested in numerous works considering upward directional solidification.

Keywords: solidification, microstructure, intermetallic, indentation, alloys

1. INTRODUCTION

Aluminum is the second most widely used metal because of its desirable chemical, physical and mechanical properties and represents an important category of technological materials [1]. Because of its high strength-to-weight ratio in addition to other properties, e.g., its appearance, non-toxicity, non-sparking and non-magnetic behavior, high corrosion resistance, and high electrical and thermal conductivities, aluminum and its alloys are used in a wide range of industrial applications with different aqueous solutions [1].

The Aluminium Association has summarized the variables that affect the mechanical properties in an aluminum alloy casting, namely, the chemical composition, solidification rate, metal soundness, and heat treatment [1]. Cast aluminum alloys mainly contain Si, Cu, and Mg as the major alloying elements [2-4]. Cu, for example, is added to Al primarily to increase the strength. Increasing the Cu content causes a continuous increase in the hardness; however, the strength and especially the ductility depend on how the Cu is distributed [5].

The Al-Cu equilibrium phase diagram is eutectic and in equilibrium with the Al_2Cu intermetallic phase at 548 °C at approximately 32 wt% copper. The extent of solution solubility at the aluminum-rich end is approximately 5.7 wt% copper. In these alloys, the Al_2Cu intermetallic phase is responsive for the high strength family of 2xx casting alloys. Commercial alloys of this type are 2219, 2011, and 2025. During solidification of these alloys, the first solid formed has a dendritic structure, and its center is composed of a low content of copper. Moving toward the outside of the arms, which corresponds to metal freezing later, the copper content increases and combines with Al to form the Al-α + Al_2Cu eutectic mixture.

After casting, these alloys are generally used in one of four conditions: as-cast, heat treated after casting, mechanically worked after casting, or worked and heat treated. In all the cases, the casting process has a significant effect upon the mechanical properties, especially in the first two cases [6]. Quaresma *et al*. [6] have reported that these properties are governed mainly by factors such as the porosity, presence of a second phase, grain cast size, and dendrite spacings. According to these authors, the improved properties of fine-grain-

*Corresponding author: otvrocha@oi.com.br or otavio.rocha@ifpa.edu.br

sized castings result from the finer distribution of microporosity and second-phase particles. In addition, the solute segregation pattern is characterized mainly by the primary and secondary dendrite spacings; moreover, the degree of microsegregation that can be obtained in a casting alloy with commercially practical homogenization treatments depends on the dendrite spacings [6-8].

Microstructural evolution during solidification depends on the alloy characteristics and is primarily a function of the temperature profiles at the solidification interface [1,6-9]. During the solidification of metallic alloys, the most frequently observed solid morphology is the dendritic microstructure [10]. The solidification parameters of alloys are the temperature gradient (G_L), growth rate (V_L) and cooling rate (T_R). These parameters directly affect the microstructure of alloy systems and significantly affect their mechanical behaviors; these effects have been intensively studied in the literature for Al-based alloys, the majority for upward and downward vertical directional solidification [1,3,4,6-33].

For vertical upward directional solidification, the effect of the convection is minimized when solute is rejected for the interdendritic regions, providing the formation of an interdendritic liquid that is denser than the global volume of liquid metal [6-9]. When the process is performed vertically downward, the system provides the melt convection that arises during the process [11]. In horizontal unidirectional solidification, when the chill is placed on the side of the mold, the convection is a function of the composition, and gradients in the liquid always occur. An interesting feature of the horizontal configuration is the gradient of the solute concentration and density in the vertical direction because solute-rich liquid falls down, whereas free solvent-crystals rise because of the buoyancy force. Moreover, a vertical temperature gradient will also arise in the sample as soon as a thermosolutal convection roll emerges. Despite these particular physical characteristics, only a few studies have reported these important effects of melt convection and the direction of growth on the columnar-to-equiaxed transformation (CET) and dendrite arm spacings for this particular case [12-14].

Realizing the effect of structural parameters on the mechanical properties of the produced material, some researchers have conducted studies that correlate the microstructure and properties, as in the 1950s, when Hall and Petch [16,17] proposed a relationship that relates the grain diameter to the hardness or yield stress of the material:

$$HV = HV_0 + k \times d^{(-1/2)} \text{ and } \sigma_e = \sigma e_0 + k \times d^{(-1/2)}, \quad (1)$$

where HV is the hardness of the material, σ_e is the yield stress, and d is the average grain size; HV_0, σe_0 and k are particular constants obtained experimentally for the material. However, for some metallic systems, the dendrite arm spacings may have a more significant effect on the resulting mechanical properties of the material than the actual grain size.

Recent studies [1,18-21] have investigated the variation of the microindentation hardness (HV) with solidification and microstructure parameters (V_L, T_R and λ_1, respectively) in Al-based alloys. In these works, the Hall-Petch power type relationship was also observed according to the following general expressions:

$$HV = C_1(V_L, T_R)^m \text{ and } HV = C_2(\lambda_1)^n, \quad (2)$$

where m and n are the exponent values relating to V_L and T_R and λ_1, respectively, and C_1 and C_2 are constants, which have been experimentally determined.

Çadırlı [1] determined for Al-(3, 6, 15, 24 and 33)wt% Cu alloys, solidified in a Bridgman system, exponent values with T_R equal to 0.09, 0.08, 0.07, 0.08 and 0.08, respectively, and with λ_1 and λ_E (E-eutectic) equal to -0.29, -0.23, -0.25, -0.25 and -0.19, respectively. Kaya *et al*. [18,20] obtained for the Al-3 wt% Cu, Al-3.0 wt% Si and Al-1.0 wt% Ti alloys [18], solidified in a Bridgman system, exponent values with V_L equal to 0.12, 0.12 and 0.14, respectively and with λ_1 equal to -0.40, -0.28 and -0.43, respectively, and for the Al-7 wt% Ni [20], also solidified in a Bridgman system, exponents of 0.26 and -0.35 with V_L and λ_1, respectively. Vasconcelos *et al*. [21] established for the Al-5.5 wt% Sn alloy, solidified in a horizontal directional solidification system under transient heat flow conditions, exponent values with V_L, T_R and λ_1 equal to 0.71, 0.13 and 0.30, respectively.

Thus, the main objective of this work is to investigate the effect of the thermal parameters (V_L and T_R), primary dendrite arm spacing (λ_1) and Al_2Cu intermetallic phase on the microhardness during transient horizontal directional solidification of Al-3 wt% Cu and Al-8 wt% Cu alloys.

2. EXPERIMENTAL PROCEDURES

The casting assembly used in the solidification experiments has been detailed in a previous article [14] and is sche-

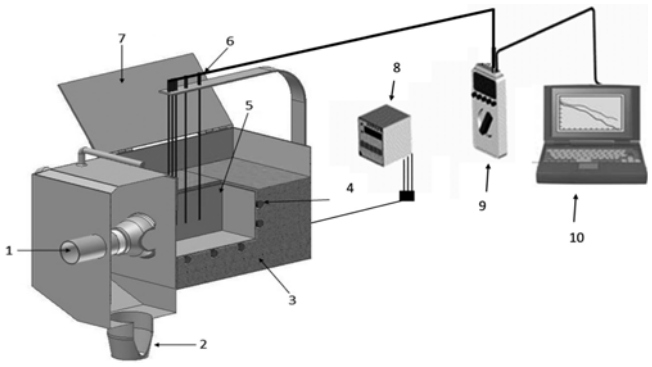

Fig. 1. Schematic representation of the horizontal experimental solidification setup: (1) water inlet, (2) water outlet, (3) insulating ceramic shielding, (4) electric heaters, (5) casting (stainless steel mold - inner wall), (6) thermocouples, (7) top cover, (8) temperature controller, (9) data logger, and (10) computer and data acquisition software.

Table 1. Casting materials used for experimentation and the corresponding thermophysical properties [7]

Properties	Density	Latent heat of fusion	Solute diffusivity	Gibbs-Thomson coefficient	Solidus temperature	Liquidus temperature	Partition coefficient	Liquidus slope
Symbol/units	ρ_S [kg/m^3] (solid) ρ_L [kg/m^3] (liquid)	L [J/kg]	D [m^2/s]	Γ [m.K]	T_S [°C]	T_L [°C]	k_O	m_L (K/wt%)
Al-3 wt% Cu	2614.6 2448.8	382849	3.5×10^{-9}	1.56×10^{-7}	548	653	0.172	3.4
Al-8 wt% Cu	2745.6 2580.0	379264	3.5×10^{-9}	1.47×10^{-7}	548	633	0.172	3.4

matically illustrated in Fig. 1. The assembly was designed in such a way that the heat was extracted only through the water-cooled system placed in the lateral mold wall, promoting horizontal directional solidification. The carbon steel mold used had a wall thickness of 3 mm, a length of 110 mm, a height of 60 mm and a width of 80 mm. The lateral inner mold surfaces were covered with a layer of insulating alumina, and the upper part of the mold was closed with refractory material to prevent heat losses. The thermal contact condition at the metal/mold interface was also standardized with the heat-extracting surface being polished.

Experiments were performed with two Al-Cu alloys (3.0 and 8.0 wt% Cu) with superheats of 10% above the *liquidus* temperature. The thermophysical properties of these alloys are based on those summarized in Table 1 [7].

During the solidification process, temperatures at different positions in the alloy samples were measured, and the data were acquired automatically. For the measurements, fine-type K thermocouples were used. The thermocouples were sheathed in 1.6-mm-diameter steel tubes and positioned at 5, 10, 15, 20, 30, 50, 70 and 90 mm for the Al-3 wt% Cu alloy and 5, 10, 15, 30, and 50 mm for the Al-8 wt% Cu alloy from the heat-extracting surface. The thermocouples were calibrated at the melting point of Al, exhibiting fluctuations of approximately 1 °C and 0.4 °C, respectively, and connected by coaxial cables to a data logger interfaced with a computer. Previous measurements of the temperature field were performed, confirming that the described experimental set-up fulfills the requirement of heat flow in the horizontal direction.

Each ingot was sectioned along its longitudinal direction, which was parallel to both the sample axis and the direction of solidification. Then, the metallographic specimens were mechanically polished with abrasive papers and subsequently etched with an acid solution composed of 5 ml of H_2O, 60 ml of HCl, 30 ml of HNO_3 and 5 ml of HF to reveal the macrostructures. A columnar-to-equiaxed transition (CET) was observed in both cases. The CET positions in the investigated alloys were clearly delineated by visual observation and optical microscopy on the etched surface, and the distances from the side of the samples were measured.

Selected transverse sections (perpendicular to the horizontal growth direction) of the directionally solidified specimens at 3, 5, 7, 10, 15, 20, 30, 40, 50, 60 and 70 mm from the metal-mold interface were polished and etched with a solution of 5% NaOH in water for micrograph examination. The image processing system Olympus BX51 and Image Tool (IT) software were used to measure the primary dendrite arm spacings (approximately 20 independent readings for each selected position, with the average taken to be the local spacing) and their distribution range. The triangle method was used for measuring these spacings on a transverse section [7,9]. One sample of each analyzed alloy was selected and subjected to X-ray diffraction (XRD) analysis. The patterns were obtained by a XRD diffractometer with a 2-theta range from 5° to 90°; Cu-Kα radiation with a wavelength, λ, of 0.15406 nm was employed.

The mechanical properties of any solidified material are usually determined using hardness, tensile, and ductility tests. The microhardness measurements in this work were performed using a Shimadzu HMV-2 model hardness measuring test device using a 100 g load and a dwell time of 10 s. The adopted Vickers microhardness values were the average of at least 20 different measurements on the transverse section of each sample. The experimental results of each microhardness value as a function of both the position and primary dendritic arm spacing are represented by a variation between the minimum and maximum limit obtained from 20 different measurements.

3. RESULTS AND DISCUSSION

The complete Al-Cu phase diagram is a complex system. Numerous intermetallic compounds are formed. Some of the phases in this system include θ-Al_2Cu, η-AlCu, γ-$AlCu_2$ and β-$AlCu_4$. In the aluminum foundry industry, there is a concern over the aluminum-rich portion and the formation of the phase θ (Al_2Cu).

Thermo-Calc software has been used to generate the partial equilibrium phase diagram, showing the most important region, which is presented in Fig. 2. The dashed lines represent the compositions used in this work. The microstructure evolution of hypoeutectic Al-Cu alloys during solidification can be divided in two stages: primary dendrite Al-phase formation (α-matrix) and the subsequent eutectic transformation with the formation of the intermetallic compound Al_2Cu (θ), being located between the interdendritic ramifications.

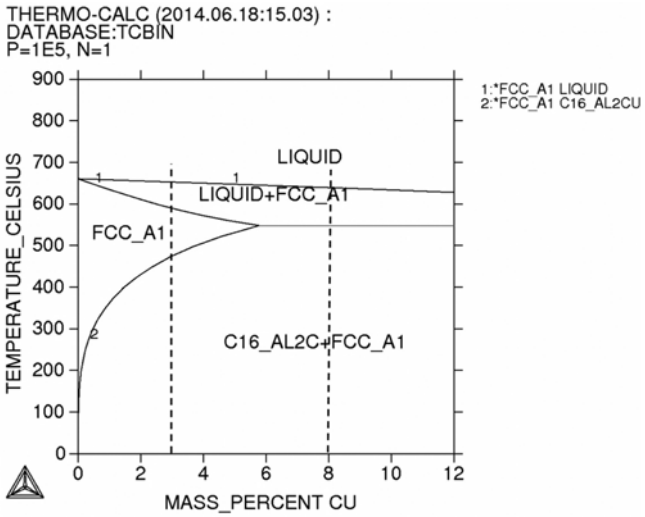

Fig. 2. Partial Al-Cu phase diagram: the dotted lines indicate the alloys examined in the present study.

Under conditions of equilibrium, the Al-3 wt% Cu alloy does not form a eutectic mixture. Fig. 3a reveals the solidifying paths, indicating the presence of an isothermal transformation temperature (T_E - eutectic temperature) of the eutectic mixture for both analyzed alloys. This transformation temperature is also observed in the experimental curves of temperature versus time for characterization of the investigated alloys in Fig. 3b.

However, in the XRD patterns in Fig. 4, the presence of α-Al and Al_2Cu phases is confirmed for both the Al-3.0 wt% Cu and Al-8.0 wt% Cu alloys.

Figures 5a and 6a present the microstructures of cross sections of samples at 5, 30 and 60 mm (Al-8.0 wt% Cu) and 5, 50 and 100 mm (Al-3.0 wt% Cu) from the metal-mold interface, showing the primary dendrite arms. The dendrite arm spacings were sufficiently distinct to make reasonably accurate measurements along the casting length. Higher amounts of the Al_2Cu phase in the interdendritic regions of the Al-8.0

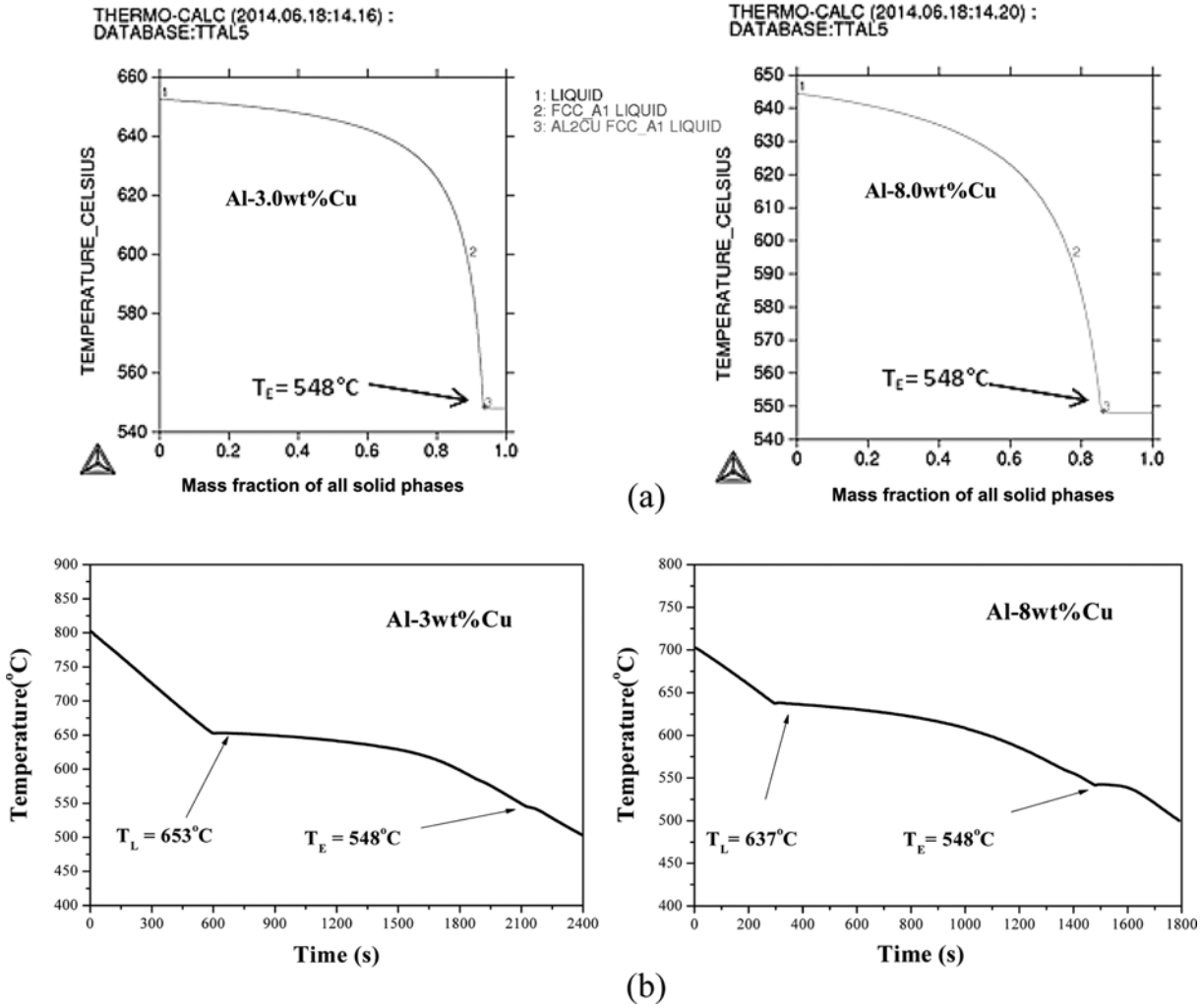

Fig. 3. (a) Solidification paths obtained by Thermo-Calc software and calculated by Sheill [34] and (b) Thermal characterization of the analyzed alloys (temperature versus time) showing the *liquidus* and *solidus* temperatures.

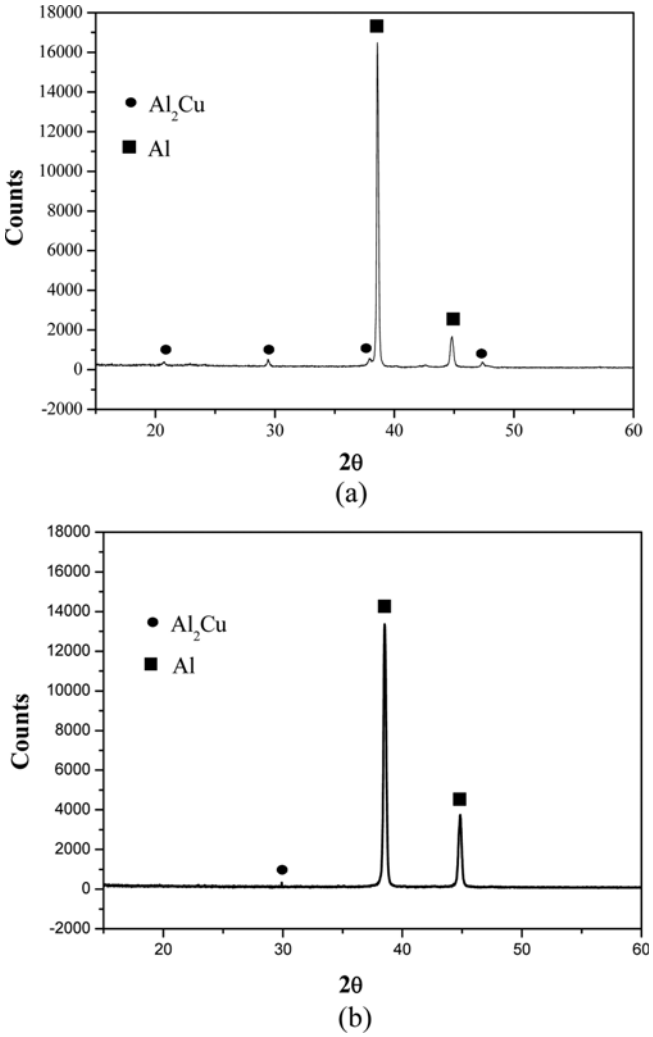

Fig. 4. Typical X-ray diffraction (XRD) patterns of (a) Al-8 wt% Cu and (b) Al-3 wt% Cu alloys for P = 40 mm.

wt% Cu alloy can be observed in Figs. 5b and 6b. In Figs. 5a and 6a, the solidification macrostructures for both studied alloys are shown. The anticipation of the columnar-to-equiaxed transition is observed for the Al-8.0 wt% Cu alloy.

Figure 7 presents the micrographs obtained by scanning electron microscopy (SEM) with the microanalysis performed using energy dispersive spectroscopy (EDS). The resulting spectra reveal the presence of an Al_2Cu-intermetallic phase between the dendritic branches, where the highest amount of this phase micro segregated in the eutectic mixture is observed for the Al-8.0 wt% Cu alloy.

Figure 8a shows the experimental cooling curves for one of the analyzed alloys for the eight thermocouples inserted into the casting during the solidification. The primary dendritic arm spacings are known to be dependent on the solidification thermal parameters such as V_L and T_R [1,3,4,6-44], all of which vary with time and position during solidification. To determine more accurate values for these parameters, the

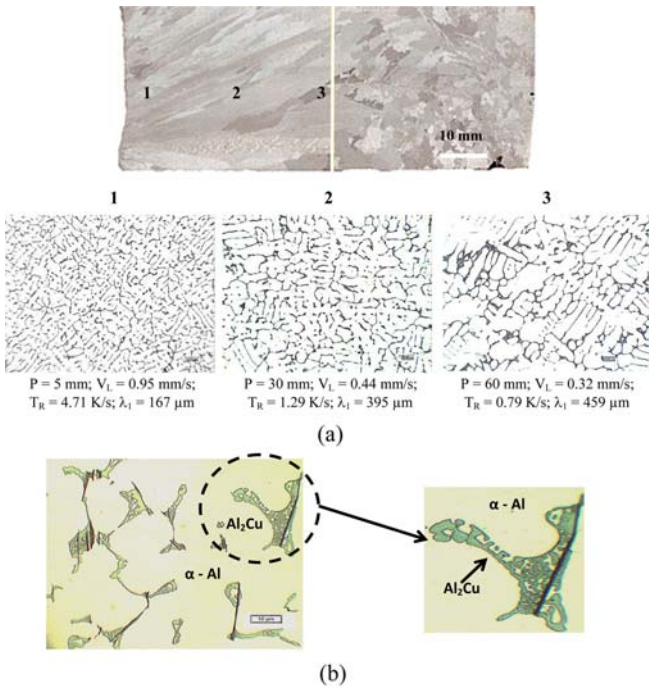

Fig. 5. Optical micrographs of directionally solidified Al-8 wt% Cu alloy: (a) cross section showing the variation in primary interdendritic spacings with the distance from the cooled stainless steel chill for distance from chill of 5 mm, 30 mm, and 60 mm, respectively; (b) cross section showing the interdendritic microsegregation of Al_2Cu intermetallic phase for distance from chill of 30 mm.

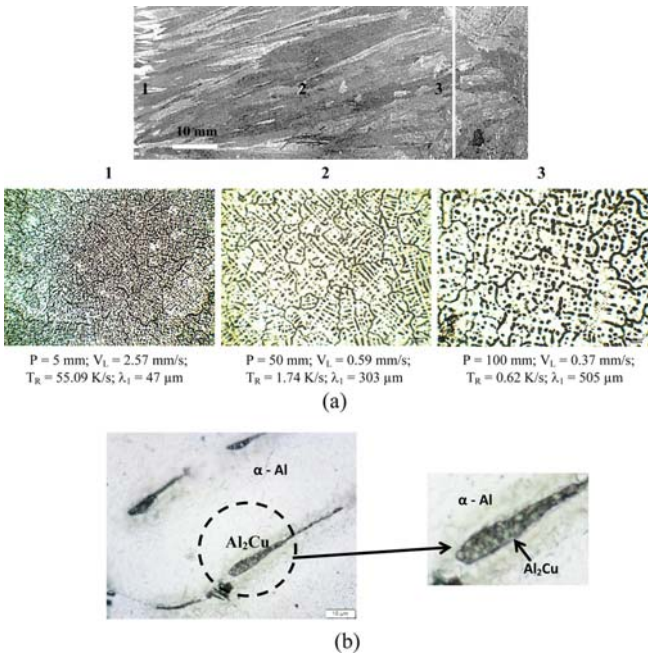

Fig. 6. Micrographs of directionally solidified Al-3 wt% Cu alloy: (a) cross section showing the variation in primary interdendritic spacings with the distance from the cooled stainless steel chill for distance from chill of 5 mm, 50 mm, and 100 mm, respectively; (b) longitudinal section showing the interdendritic microsegregation of Al_2Cu intermetallic phase for distance from chill of 30 mm.

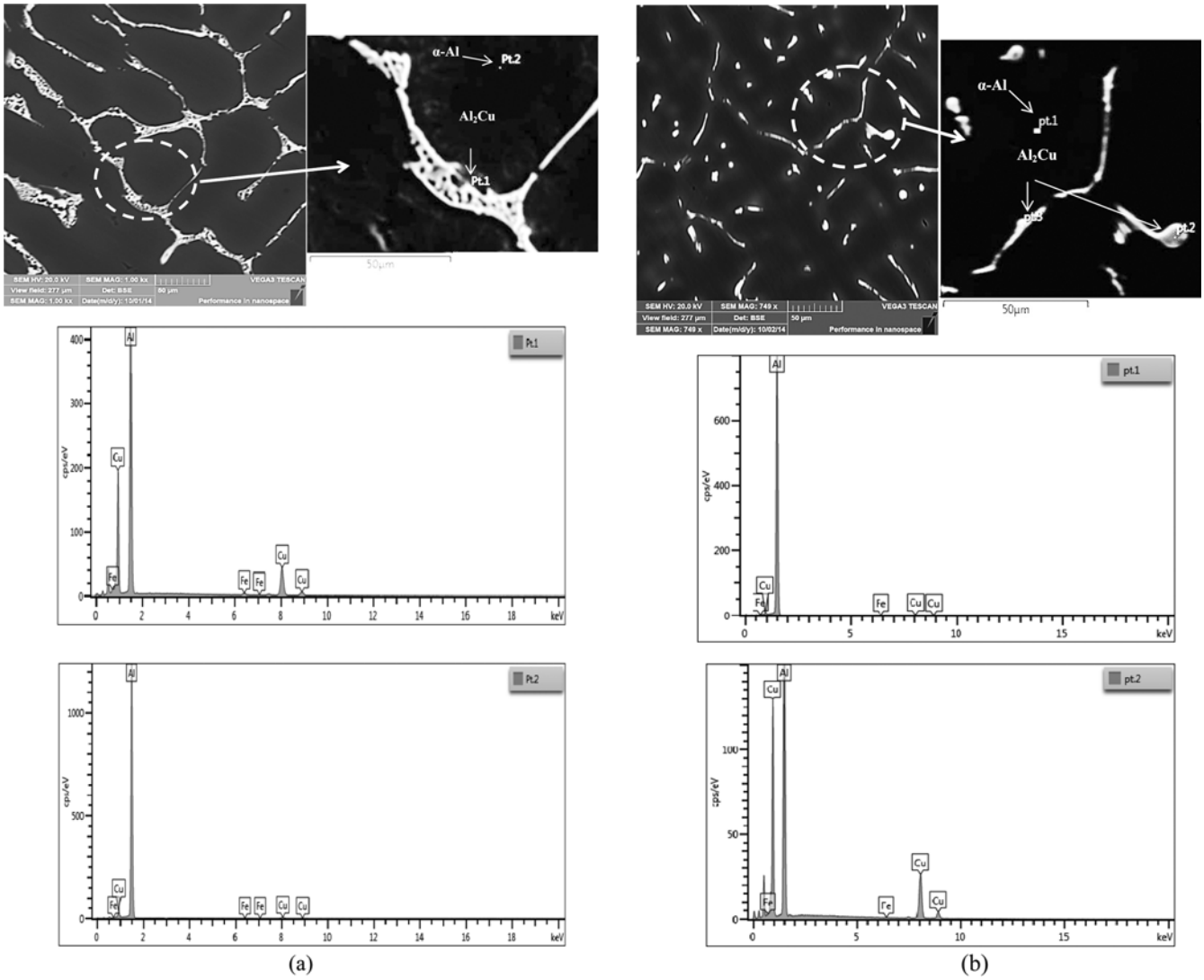

Fig. 7. SEM micrographs and microanalysis by energy dispersive spectroscopy (EDS) of the analyzed alloys: (a) Al-8 wt% Cu and (b) Al-3 wt% Cu.

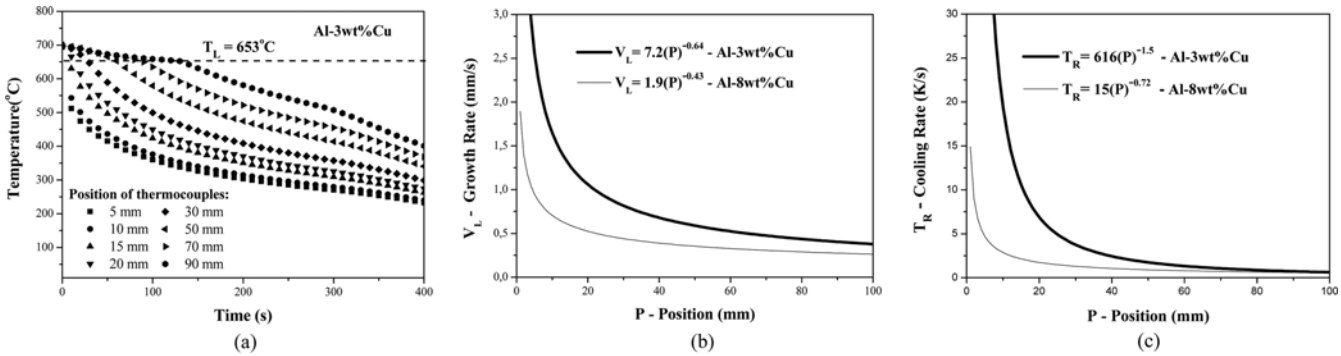

Fig. 8. (a) Experimental cooling curves at different positions along the casting length during the directional solidification of the Al-3 wt% Cu alloy. T_L is the *liquidus* temperature, (b) growth rate, and (c) cooling rate as function of the *liquidus* isotherm position.

results of experimental thermal analysis have been used to determine the displacement of the *liquidus* isotherm, i.e., the thermocouple readings are used to generate a plot of position from the metal-mold interface as a function of time corresponding to the *liquidus* front passing by each thermocouple. A curve fitting technique on such experimental points gen-

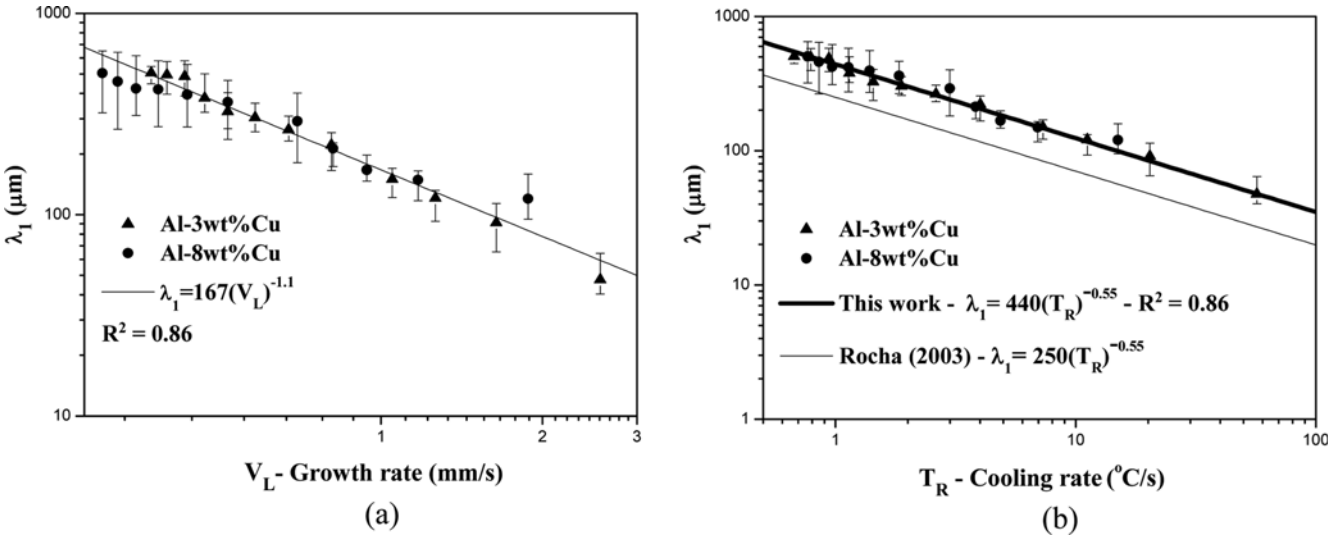

Fig. 9. Experimental primary dendrite arm spacings for the analyzed alloys as a function of (a) growth rate and (b) cooling rate.

erates power functions of position as a function of time. The derivative of this function with respect to time yields values for V_L. The T_R profile is calculated by considering the thermal data recorded immediately after the passing of the *liquidus* front by each thermocouple. The method used for measuring the tip cooling rate has been detailed by Rocha *et al*. and Sá *et al*. [8,23-25]. Figs. 8b and 8c plot the experimental growth and cooling rates as a function of the *liquidus* isotherm position, i.e., $(V_L, T_R) = f(P)$.

Figures 9a and 9b show the power-type experimental laws represented by $\lambda_1 = C_1 (V_L)^{-1.1}$ and $\lambda_1 = C_2 (T_R)^{-0.55}$ obtained for both alloys studied in this work. The same values of C_1 and C_2 equal to 167 and 440, respectively, have been observed for the Al-3.0 wt% Cu and Al-8.0 wt% Cu alloys, which characterize the experimental variation of the primary dendrite arm spacing as a function of V_L and T_R. These results are consistent with observations reported by Carvalho *et al*. [15], Peres *et al*. [25] and Rocha *et al*. [7], who claim that exponential relationships $\lambda_1 = \text{constant} (V_L)^{-1.1}$ and $\lambda_1 = \text{constant} (T_R)^{-0.55}$ best generate the experimental variation of the primary dendritic arm spacings with the growth rate and cooling rate along the transient solidification of binary Al-Si (horizontal solidification, upward and downward vertical solidification) and Al-Cu (upward vertical solidification) alloys, respectively. The same power-type experimental laws verified in this work have also been observed in the literature for other systems of non-ferrous alloys independent of the growth direction. Table 2 summarizes the experimental results from the literature. These results reinforce the proper application of the exponent -0.55 to correlate the primary dendrite arm spacing evolution with the cooling rate for every non-ferrous alloy systems.

A comparison between the experimental growth law obtained in this study and another law in the literature for upward directionally solidified Al-Cu alloys is presented in Fig. 9b. For the horizontal system, higher values of the primary dendrite arm spacing are needed to fix the *liquidus* isotherm position on the axis of abscissa. This finding may be associated with the convective effect of solute-rich liquid flow and with the effect of the direction of the gravity vector, which is perpendicular to the direction of advance of the solidification interface.

Figure 9 shows the dependence of the microhardness (HV) on the distance (P) from the metal-mold interface (Fig. 9a) as well as the effect of the thermal parameters V_L and T_R (Figs. 9b and 9c) for the investigated alloys. HV decreases with the advance of the *liquidus* isotherm (P) and increases to higher

Table 2. Experimental laws for predicting primary dendritic arm spacing for Al-based binary and multicomponent alloys, considering transient directional solidification

Growth direction	Alloy	Experimental law	Ref.
Upward	Al-Cu	$\lambda_1 = 250(T_R)^{-0.55}$	[7]
Upward	Al-Si	$\lambda_1 = 220(T_R)^{-0.55}$	[25]
Downward		$\lambda_1 = 85(T_R)^{-0.55}$	[29]
Horizontal		$\lambda_1 = 90(T_R)^{-0.55}$	[12]
Upward	Al-Sn	$\lambda_1 = 70(T_R)^{-0.55}$	[28]
Horizontal		$\lambda_1 = 144(T_R)^{-0.55}$	[21]
Upward	Al-Ni	$\lambda_1 = 100(T_R)^{-0.55}$	[26]
		$\lambda_1 = 220(T_R)^{-0.55}$	
Upward	Al-Fe	$\lambda_1 = 95(T_R)^{-0.55}$	[30]
Upward	Al-Cu-Si	$\lambda_1 = 153(T_R)^{-0.55}$	[31]
Upward	Sn-Pb	$\lambda_1 = 80.5(T_R)^{-0.55}$	[7]
		$\lambda_1 = 44(T_R)^{-0.55}$	
		$\lambda_1 = 25(T_R)^{-0.55}$	
Downward		$\lambda_1 = 27(T_R)^{-0.55}$	[32]
Upward	Pb-Sb	$\lambda_1 = 115(T_R)^{-0.55}$	[27]
Upward	Zn-Cu	$\lambda_1 = 55(T_R)^{-0.55}$	[33]
		$\lambda_1 = 34(T_R)^{-0.55}$	

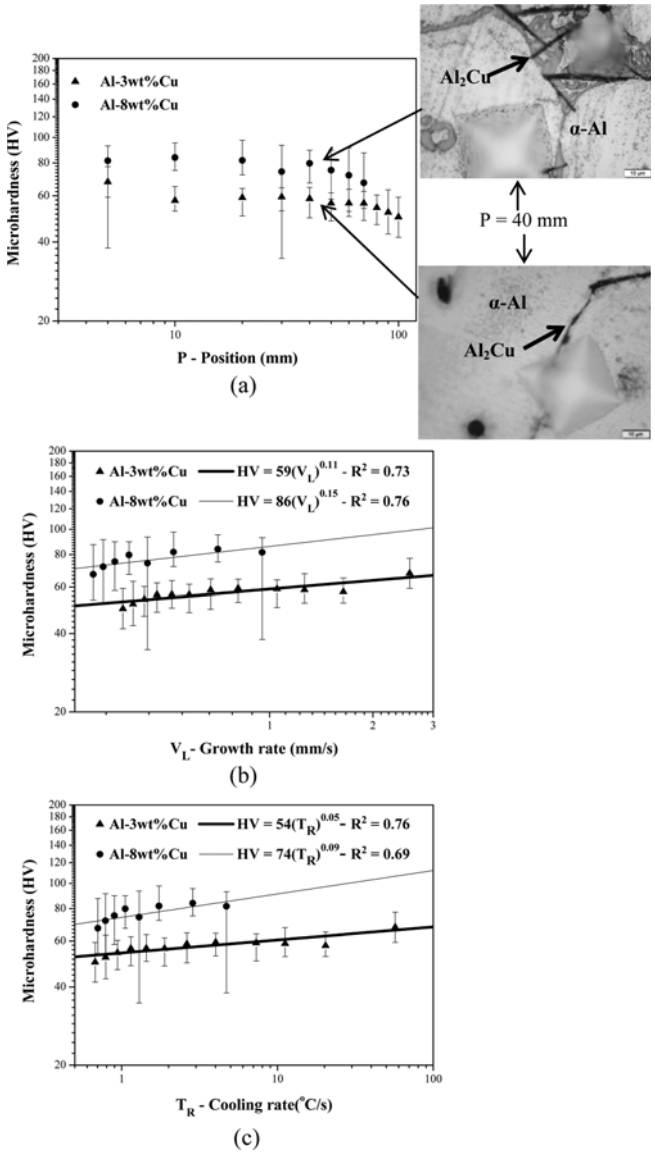

Fig. 10. Microhardness evolution for the analyzed alloys as a function of (a) *liquidus* isotherm position (P), (b) growth rate (V_L), and (c) cooling rate (T_R).

values of V_L and T_R. The association of HV with V_L and T_R can be represented by power- and Hall-Petch-type laws given by $HV = 59(V_L)^{0.11}$ and $HV = 54(T_R)^{0.05}$ and $HV = 86(V_L)^{0.15}$ and $HV = 74(T_R)^{0.09}$ for Al-3 wt% Cu and Al-8 wt% Cu alloys, respectively.

In Fig. 9a, images of the HV microindentations obtained for both studied alloys at 40 mm and the corresponding values of the microhardness are presented. The effect of the Al_2Cu intermetallic phase contained in the eutectic region of higher concentration of Cu increasing the microhardness values is clearly observed.

Figure 10 depicts the evolution of HV with the measured primary dendrite arm spacings along the casting length. The microhardness results decrease with an increase in the λ_1 values, and the dependence of HV on λ_1 and $\lambda_1^{-1/2}$ can also be represented by power- and Hall-Petch-type equations given by $HV = 97(\lambda_1)^{-0.098}$ and $HV = 47+147(\lambda_1)^{-1/2}$ and $HV = 151(\lambda_1)^{-0.12}$

Table 3. The relationships among microhardness, growth rate, cooling rate and primary dendrite arm spacings for investigated alloys in this work and comparison with values obtained in the literature for the Al-3 wt% Cu alloy

Alloy	Experimental law (this work)	Steady state upward solidification	Ref.
Al-3.0 wt% Cu	$HV = 59(V_L)^{0.11}$ $HV = 54(T_R)^{0.05}$ $HV = 97(\lambda_1)^{-0.098}$	$HV = 72.1(T_R)^{0.09}$ $HV = 41.5(\lambda_1)^{-0.29}$ $HV = 88.32(V_L)^{0.12}$ $HV = 33.14(\lambda_1)^{-0.40}$	[1]
	$HV = 47+147(\lambda_1)^{-1/2}$	-	[18]
Al-8.0 wt% Cu	$HV = 86(V_L)^{0.15}$ $HV = 74 (T_R)^{0.09}$ $HV = 151(\lambda_1)^{-0.12}$ $HV = 60+270(\lambda_1)^{-1/2}$	-	-

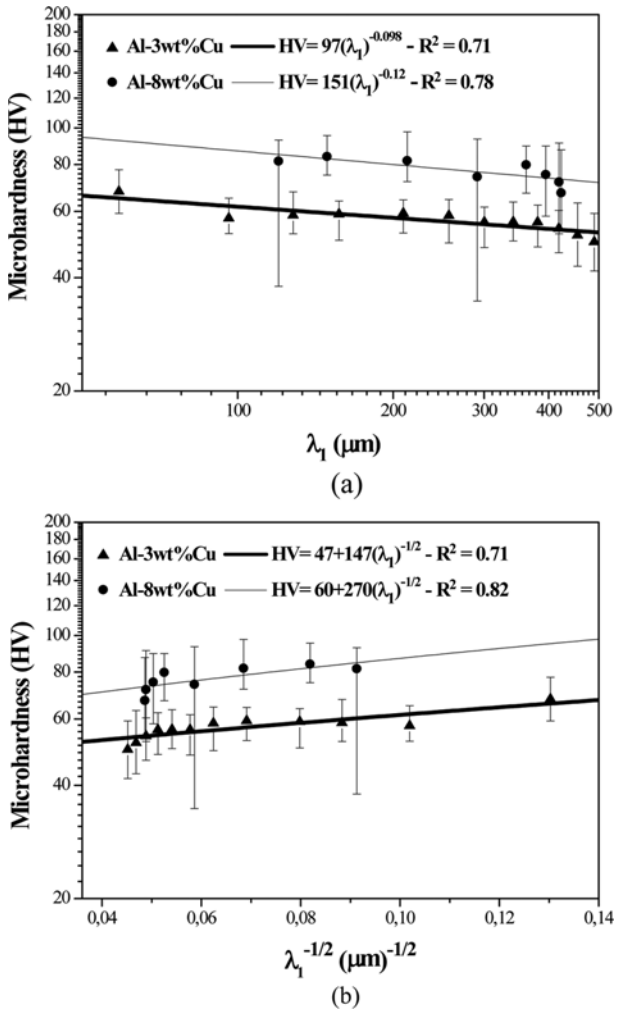

Fig. 11. Microhardness evolution as a function of primary dendrite arm spacings: (a) λ_1 and (b) $\lambda_1^{-1/2}$.

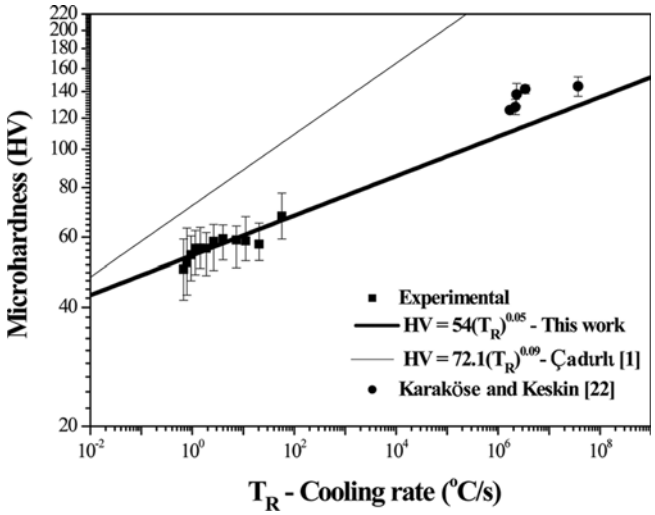

Fig. 12. Comparison between the results obtained in this work with those obtained by Çadırlı [1] and Karaköse and Keskin [22].

and HV = 60+270$(\lambda_1)^{-1/2}$ for Al-3 wt% Cu and Al-8 wt% Cu alloys, respectively.

Table 3 presents the consolidated results of HV = f (V_L, T_R, λ_1 and $\lambda_1^{-1/2}$) for both alloys compared with others results from the literature developed for the Al-3 wt% Cu alloy solidified under steady-state conditions of heat extraction. Figure 11 compares the power-type experimental law obtained for the Al-3 wt% Cu alloy of the present study with the experimental laws proposed by Çadırlı [1] and Karaköse and Keskin [22]. A reasonable approximation of the compared laws to high and low cooling rates was observed. It is emphasized that the cooling rates applied in these studies were between 0.01 and 4 K/s and 1.7×10^6 to 3.7×10^7 K/s for the works presented by Çadırlı [1] and Karaköse and Keskin [22], respectively.

To perform a theoretical and experimental analysis, in Fig. 13, the present experimental results are compared with the theoretical predictions furnished by the main predictive models existing in the literature, the Bouchard-Kirkaldy (BK) [35] and Hunt-Lu (HL) [36] models, concerning the growth of primary spacings in transient conditions. These models have been validated for the majority of binary alloys solidified upward directionally [6,9,11,23,25-32,37-44]. It is possible to observe a good approximation between the experimental results of this work with the theoretical values of the BK model as well as the maximum theoretical values of the HL model. The BK model depends additionally on an empirical dimensionless calibration parameter, a_1, for primary spacings. These authors, based mainly on experimental results of a single article from the literature [35] have proposed a_1 to equal 250 for Al alloys.

4. CONCLUSIONS

Experiments were conducted to analyze the effect of thermal parameters, the primary dendrite arm spacing and the Al2Cu intermetallic phase on the microhardness during the horizontal transient directional solidification of Al-3 wt% Cu and Al-8 wt% Cu alloys. The following major conclusions are derived from the present study:

(1) Under transient conditions, the primary dendrite arm spacings (λ_1) were observed to decrease with an increase in the thermal parameters (V_L - growth rate and T_R - cooling rate);

(2) In both cases, the same power-type experimental laws were observed to associate the primary dendrite arm spacings with V_L and T_R given by $\lambda_1 = 167(V_L)^{-1.1}$ and $\lambda_1 = 440(T_R)^{-0.55}$, respectively. These results reinforce the proper application of the exponent -0.55 to correlate the primary dendrite arm spacing evolution with the cooling rate for every non-ferrous alloy system solidified under transient directional solidifica-

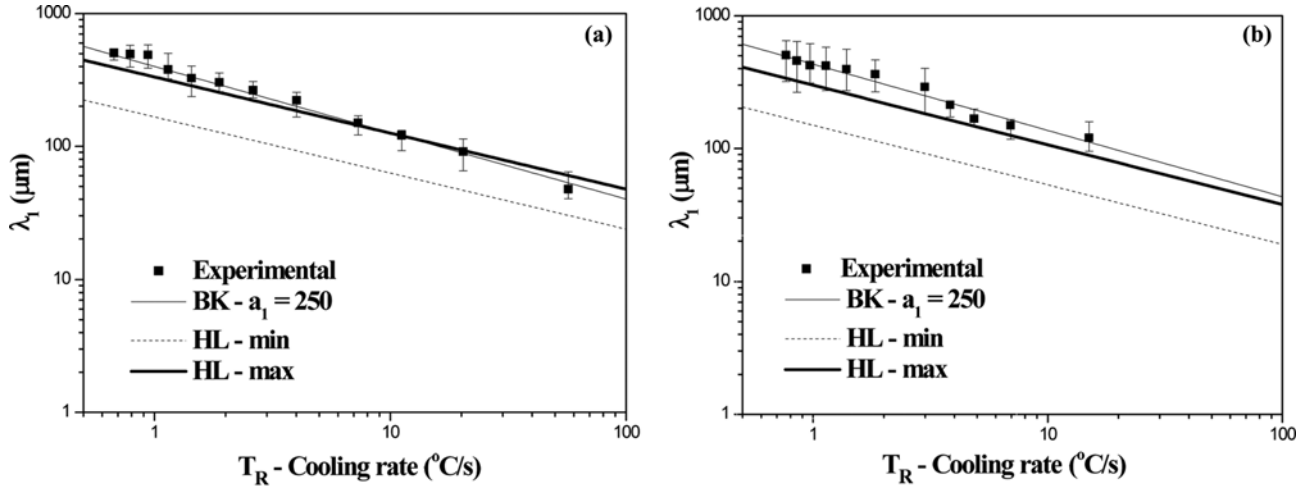

Fig. 13. Comparison of experimental and theoretical primary dendrite arm spacings as a function of cooling rate for the investigated alloys in transient horizontal directional solidification. (a) Al-3 wt%Cu and (b) Al-8 wt%Cu.

tion conditions;

(3) The microhardness (HV) dependency on the thermal parameters and microstructure can be represented by power- and Hall-Petch-type relationships given by $HV = 59(V_L)^{0.11}$, $HV = 54(T_R)^{0.05}$, $HV = 97(\lambda_1)^{-0.098}$ and $HV = 47+147(\lambda_1)^{-1/2}$ for Al-3 wt% Cu and $HV = 86(V_L)^{0.15}$, $HV = 74(T_R)^{0.09}$, $HV = 151(\lambda_1)^{-0.12}$ and $HV = 60+270(\lambda_1)^{-1/2}$ for Al-8 wt% Cu alloys;

(4) The X-Ray diffraction (XRD) results as well as the observations made in the interdendritic eutectic mixture clearly reveal larger amounts of the Al_2Cu intermetallic phase between the dendrite arms, which appear to result in the higher HV values obtained for the Al-8 wt% Cu alloy;

(5) The comparison between power-type experimental laws that associate HV with T_R reveals that the law obtained for the Al-3 wt% Cu alloy solidified under transient horizontal directional conditions satisfactorily represents the laws proposed in the literature for low and high cooling rates.

(6) Theoretical models from the literature have been proposed to predict primary dendrite arm spacing in alloys directionally solidified under transient conditions, which have been applied in the majority of studies that consider the upward solidification. A good approximation was observed between the experimental results obtained for the primary dendrite arm spacings in this work and those calculated using the BK model as well as the theoretical values of the upper limit obtained using the HL model.

ACKNOWLEDGMENTS

The authors acknowledge the financial support provided by IFPA (Federal Institute of Education, Science and Technology of Pará), UFPA (Federal University of Pará), CAPES (Coordination of Superior Level Staff Improvement) and CNPq (the Brazilian Research Council), Brazil.

REFERENCES

1. E. Çadırlı, *Met. Mater. Int*. **19**, 411 (2013).
2. E. Sjölander, Ph.D. *Thesis*, pp.1-45, School of Engineering, Jönköping University Jönköping, Sweden (2011).
3. M. Tash, F. H. Samuel, F. Mucciardi, and H. W. Doty, *Mater. Sci. Eng. A* **443**, 185 (2007).
4. E. Ozbakir, *Ms. Sci. Thesis*, pp.1-98, McGill University, Montréal Québec, Canada (2008).
5. G. E. Totten and S. D. MacKenzie, *Handbook of Aluminum: Physical Metallurgy and Processes*, p.724, Marcel Dekker, New York (2003).
6. J. M. V. Quaresma, C. A. Santos, and A. Garcia, *Metall. Mater. Trans. A* **31**, 3167 (2000).
7. O. L. Rocha, C. A. Siqueira, and A. Garcia, *Metall. Mater. Trans. A* **34**, 995 (2003).
8. A. Geying and L. Lixin, J. Cryst. Growth **80**, 383 (1987).
9. M. Gündüz and E. Çadırlı, *Mater. Sci. Eng. A* **327**, 167 (2002).
10. R. Trivedi and W. Kurz, *Int. Mater. Rev.* **39**, 49 (1994).
11. J. E. Spinelli, I. L. Ferreira, and A. Garcia, *J. Alloys Compd.* **384**, 217 (2004).
12. D. B. Carvalho, E. C. Guimarães, A. L. Moreira, D. J. Moutinho, J. M. D. Filho, and O. L. Rocha, *Mater. Res*. **16**, 874 (2013).
13. J. N. Silva, D. J. Moutinho, A. L. Moreira, I. L. Ferreira, and O. L. Rocha, *Mater. Chem. Phys*. **130**, 179 (2011).
14. J. N. Silva, D. J. Moutinho, A. L. Moreira, I. L. Ferreira, and O. L. Rocha, *J. Alloys Compd*. **478**, 358 (2009).
15. D. B. Carvalho, A. L. Moreira, D. J. Moutinho, J. M. Filho, O. L. Rocha, and J. E. Spinelli, *Mater. Res*. **17**, 498 (2013).
16. E. O. Hall, *Proc. Phys. Soc. B* **64**, 742 (1951).
17. N. J. Petch, *J. Iron Steel Inst. Lond*. **174**, 25 (1953)
18. H. Kaya, E. Çadırlı, U. Böyük, and N. Maraslı, *Appl. Surf. Sci.* **255**, 3071 (2008).
19. H. Kaya, U. Böyük, E. Çadırlı, and N. Maraslı, *Mater. Design* **34**, 707 (2012).
20. H. Kaya, U. Böyük, E. Çadırlı, and N. Marasli, *Met. Mater. Int*. **19**, 39 (2013).
21. A. J. Vasconcelos, C. V. A. Silva, A. L. S. Moreira, M. P. S. Silva, and O. L. Rocha, *R. Esc. Minas* **67**, 173 (2014).
22. E. Karaköse and M. Keskin, *Mater. Design* **32**, 4970 (2011).
23. O. L. Rocha, C. A. Siqueira, and Garcia, A. *Mater. Sci. Eng. A* **361**, 111 (2003).
24. F. Sá, O. L. Rocha, C. A. Siqueira, and A. Garcia, *Mater. Sci. Eng. A* **373**, 131 (2004).
25. M. D. Peres, C. A. Siqueira, and A. Garcia, *J. Alloys Compd.* **381**, 168 (2004).
26. M. V. Canté, J. E. Spinelli, N. Cheung, and A. Garcia, *Met. Mater. Int*. **16**, 39 (2010).
27. D. M. Rosa, J. E. Spinelli, I. L. Ferreira, and A. Garcia, *Metall. Mater. Trans. A* **39**, 2161 (2008).
28. K. S. Cruz, E. S. Meza, F. A. P. Fernandes, J. M. V. Quaresma, L. C. Casteletti, and A. Garcia, *Metall. Mater. Trans. A* **41**, 972 (2010).
29. J. E. Spinelli, M. D. Peres, and A. Garcia, *J. Alloys Compd.* **403**, 228 (2005).
30. P. R. Goulart, *Ph. D. Thesis*, pp.1-123, University of Campinas, Campinas, Brazil (2010).
31. I. L. Ferreira, D. J. Moutinho, L. G. Gomes, O. L. Rocha, P. R. Goulart, and A. Garcia, *Mater. Sci. Forum* **636-637**, 643 (2010).
32. J. E. Spinelli, I. L. Ferreira, and A. Garcia, *J. Alloys Compd*. **384**, 217 (2004).
33. C. Brito, C. A. Siqueira, J. E. Spinelli, and A. Garcia, *J. Phys. Chem. Solids* **73**, 1173 (2012).
34. E. Scheil, *Z. Metallkunde*. **34**, 70 (1942).
35. D. Bouchard and J. S. Kirkaldy, *Metall. Mater. Trans. B* **28**, 651 (1997).
36. J. D. Hunt and S. Z. Lu, *Metall. Mater. Trans. A* **27**, 611 (1966).
37. E. Çadırlı and M. Gündüz, *J. Mater. Sci.* **35**, 3837 (2000).
38. L. Yu, G. L. Ding, J. Reye, S. N. Ojha, and S. N. Tewari, *Metall. Mater. Trans. A* **30**, 2463 (1999).

39. S. P. O'Dell, Ding G. L. and S. N. Tewari, *Metall. Mater. Trans. A* **30**, 2159 (1999).
40. X. Wan, Q. Han, and J. D. Hunt, *Acta Mater.* **45**, 3975 (1997).
41. G. Ding, W. Huang, X. Lin, and Y. Zhou, *J. Cryst. Growth* **177**, 281 (1997).
42. J. Feng, W.D. Huang, X. Lin, Q.Y. Pan, T. Li, and Y. H. Zhou, *J. Cryst. Growth* **197**, 393 (1999).
43. X. Lin, W. Huang, J. Feng, T. Li, and Y. H. Zhou, *Acta Mater.* **47**, 3271 (1999).
44. N. Tiedje, P. N. Hansen, and A. S. Pedersen, *Metall. Mater. Trans. A* **27**, 4084 (1996).